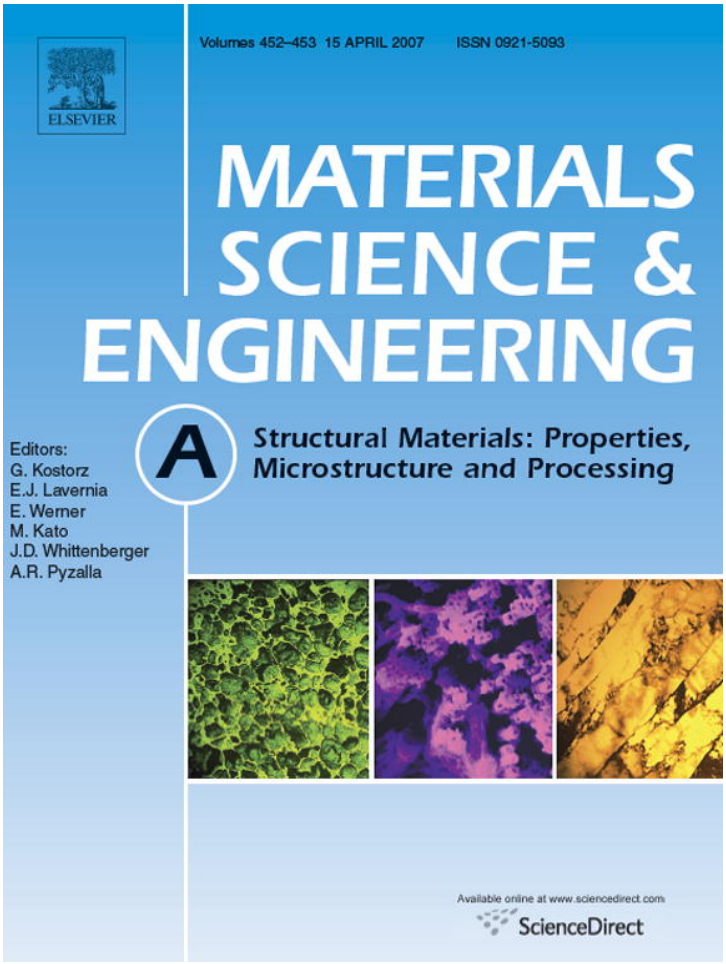

ELSEVIER

Materials Science and Engineering A 452–453 (2007) 633–639

MATERIALS SCIENCE & ENGINEERING A

www.elsevier.com/locate/msea

Elastic constants and internal friction of martensitic steel, ferritic-pearlitic steel, and α-iron

Sudook A. Kim *, Ward L. Johnson

National Institute of Standards and Technology, Materials Reliability Division, 325 Broadway, Boulder, CO 80305, USA

Received 4 August 2006; received in revised form 23 October 2006; accepted 29 November 2006

Abstract

The elastic constants and internal friction of induction hardened and unhardened SAE 1050 plain-carbon steel at ambient temperatures were determined by resonant ultrasonic spectroscopy. The hardened specimen contained only martensite and the unhardened specimen was ferrite-pearlite. Using an inverse Ritz algorithm with assumed orthorhombic symmetry, all nine independent elastic-stiffness coefficients were determined, and, from the resonance peak widths, all nine components of the internal-friction tensor were determined. Similar measurements and analysis on monocrystalline α-iron were performed. The steel has slight elastic anisotropy, and the isotropically approximated elastic moduli were lower in the martensite than in ferrite-pearlite: shear modulus by 3.6%, bulk modulus by 1.2%, Young modulus by 3.2%, and Poisson ratio by 1.5%. Isotropically approximated elastic moduli of α-iron were 0.6–1.3% higher than ferrite-pearlite. All components of the internal-friction in martensite were higher than those of ferrite-pearlite, but lower than those of α-iron.

Keywords: α-Iron; Bulk modulus; Carbon steel; Damping; Elastic constants; Ferrite; Hardness; Induction hardening; Internal friction; Martensite; Iron; Pearlite; Plain steel; Poisson ratio; Resonant ultrasound spectroscopy; Shear modulus; Young modulus

1. Introduction

The elastic moduli of martensitic and ferritic-pearlitic plain carbon steel play a central role in determining the other mechanical properties of induction-hardened parts, including crack resistance arising from compressive residual stress at hardened surfaces. Nevertheless, published experimental measurements of moduli rarely have included both martensitic and ferritic-pearlitic states of a single alloy. Variations in reported values for alloys with similar composition also are significant. In this report, we present resonant ultrasonic measurements of the complete elastic-constant and internal-friction tensors of martensitic and a ferritic-pearlitic plain carbon steel, SAE 1050, which has a medium carbon content of ∼0.5 wt.%. To interpret the results, we also present measurements on monocrystalline body-centered-cubic iron.

2. Specimens

We extracted two steel specimens from commercially fabricated automotive drive shafts that were induction heated, water quenched to intermediate temperatures, and, then, slowly cooled to ambient temperatures. The material was hot-rolled SAE 1050 steel with composition, in weight percent, of 0.48–0.55 C, 0.9–1.1 Mn, 0.15–0.30 Si, 0.3 Al, <0.05 S, <0.04 P, <0.10 Ni, <0.12 Cr, <0.05 Mo, and <0.18 Cu. The shafts had several grooves and splines machined in the surface, as described elsewhere [1], but the regions from which specimens were taken had a uniform diameter of 23.8 mm. Fig. 1 shows the hardness through surface depths of the two shafts, which are labeled B564 and C322. The Rockwell-C hardness (R_C) values were derived from microficial hardness data that were provided by the manufacturer.

Specimen B564 showed 58 R_C hardness extending to a depth of 3.2 mm from the surface. From this fully hardened region, a rectangular-parallelepiped specimen was made. The dimensions of this specimen were 3.1 mm × 2.8 mm × 2.9 mm, corresponding to the radial, azimuthal, and axial directions, respectively, of the cylinder. A second specimen, taken from

* Corresponding author. Tel.: +1 303 497 3424; fax: +1 303 497 5030.
E-mail address: sak430@boulder.nist.gov (S.A. Kim).

0921-5093/$ – see front matter © 2006 Elsevier B.V. All rights reserved.
doi:10.1016/j.msea.2006.11.147

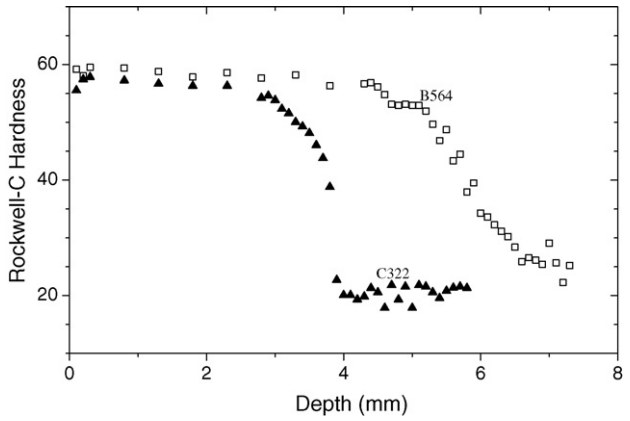

Fig. 1. Hardness vs. depth in induction-hardened shafts. Specimens were taken from regions of nearly constant hardness.

the unhardened center of the shaft C322, had dimensions of 10.7 mm × 9.32 mm × 12.1 mm and an average hardness of 20 R_C. A third specimen was α-Fe with dimensions of 4.3 mm × 5.2 mm × 4.6 mm and crystallographic directions [1 0 0], [0 1 0], and [0 0 1] aligned perpendicular to the rectangular faces. Opposite surfaces of the specimens were parallel within 8 μm.

We determined mass densities by Archimedes' method using distilled water as a standard. The densities of martensite, ferrite-pearlite, and α-iron were 7.709 ± 0.002 g/cm^3, 7.835 ± 0.001 g/cm^3, and 7.851 ± 0.011 g/cm^3, respectively.

3. Methods

To study elastic stiffness and internal friction of these materials, we used resonant ultrasonic spectroscopy, which has been described in detail elsewhere [2]. Briefly, a piezoelectric transducer produces a sinusoidal vibration at one point on a specimen, and another piezoelectric transducer detects the response of the specimen at a different point. One implementation employs a tripod arrangement, as shown in Fig. 2(a), with the third element acting only to support the specimen. This arrangement was used on the ferrite-pearlite specimen (C322), which had a mass that was large enough to produce sufficient acoustic coupling between the specimen and transducers. For the two smaller specimens, the arrangement shown in Fig. 2(b) was used. The transducers held the specimen by diagonal corners with spring forces that are set low to minimize damping from the mechanical contact. Resonant ultrasonic spectroscopy typically introduces only slight perturbations to the resonance by mechanical contact. In contrast, the more commonly employed method of pulse-echo superposition requires measurements using bonded transducers with more than one orientation and/or polarization, and more than one specimen often is needed to obtain the complete set of elastic constants.

We determined elastic stiffness coefficients C_{ij} using an inverse Ritz analysis [2–4], which requires measured resonant frequencies, specimen shape, mass density, dimensions, and initial realistic guesses for the C_{ij}. The elastic symmetries of the specimens were assumed to be orthorhombic for both hardened

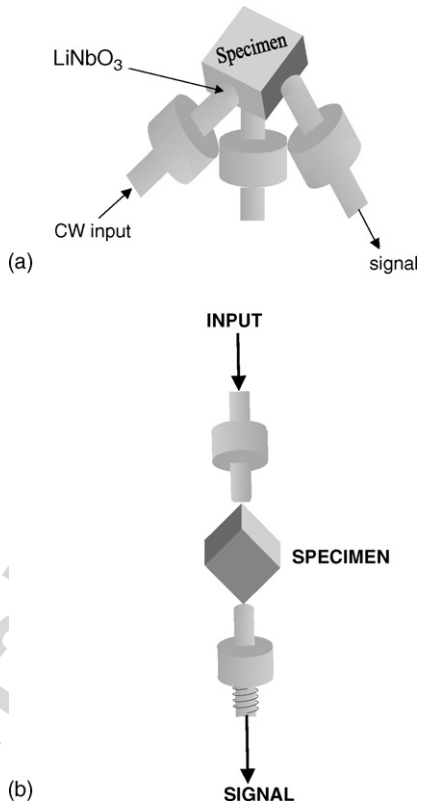

Fig. 2. (a) Tripod specimen holder. One transducer sends a continuous sinusoidal signal with varying frequency, one transducer detects macroscopic resonant frequencies, and the third transducer supports the specimen. Semispherical buffer rods provide a point contact with the specimen. (b) Spring-loaded specimen holder. The fixture holds the specimen at opposite corners to minimize the contact loss.

and unhardened specimens. For each resonance frequency f_n, an internal friction q_n^{-1} also was determined from the full width of the peak δf at $1/\sqrt{2}$ of maximum: $q_n^{-1} = \delta f / f_n$.

The elastic stiffness and internal friction can be considered to be the real and imaginary parts of a complex elastic stiffness tensor $\tilde{C}_{ij}$: $\tilde{C}_{ij} = C_{ij}(1 + iQ_{ij}^{-1})$. The q_n for a given resonance is a function of several components of the internal friction tensor Q_{ij}^{-1}. Following successful convergence of the inverse Ritz analysis, the Q_{ij}^{-1} were determined by solving a set of simultaneous equations,

$$Q_{ij\,\mathrm{calc.}}^{-1} = \left(J_{nij}^{t}\, J_{nij}\right)^{-1} J_{nij}^{\mathrm{t}}\, q_n^{-1}, \tag{1}$$

where $J_{nij} = 2(C_{ij}/f_n)(\partial f_n/\partial C_{ij})$, J_{nij}^{t} is the transpose of J_{nij}, and $\partial f_n/\partial C_{ij}$ denotes the variation of resonance frequency with respect to the elastic stiffness. Q_{ij}^{-1} is assumed to have no significant dependence on frequency over the measured range. The validity of this assumption is considered below.

In order to compare the elastic stiffnesses of orthorhombic (nine $\tilde{C}_{ij}$) martensitic and ferrite-pearlite steels with those of α-Fe (three $\tilde{C}_{ij}$), all $\tilde{C}_{ij}$ were converted into sets of isotropic elastic moduli (two $\tilde{C}_{ij}$). The orthorhombic elastic coefficients were converted to shear modulus $\tilde{G}$ and bulk modulus $\tilde{B}$ using the Voigt-Reuss-Hill model [5]. For the cubic elastic stiffness coefficients, the corresponding isotropic shear modulus was cal-

culated using Kröner's model [6,7], which agrees best with the observations made in copper, and the bulk modulus was calculated from the relation $\tilde{B} = (\tilde{C}_{11} + 2\tilde{C}_{12})/3$. $\tilde{G}$ and $\tilde{B}$ relate to the Young modulus $\tilde{E}$, longitudinal modulus $\tilde{C}_l$, and Poisson ratio ν through

$$\tilde{E} = \frac{9\tilde{B}\tilde{G}}{3\tilde{B} + \tilde{G}}, \tag{2}$$

$$\tilde{C}_l = \tilde{B} + \tfrac{4}{3}\tilde{G}, \tag{3}$$

$$\nu = \frac{1}{2}\frac{3B - 2G}{3B + G}, \tag{4}$$

4. Results

The induction hardening resulted in growth of grains in the outer section of the shaft during heating to the austenitic phase region. Then, the material transformed from austenite into the martensitic structure during subsequent rapid water quenching. Fig. 3 shows the microstructure of the unhardened core, specimen C322, which contains a mixture of ferrite (white areas) and pearlite. Most of the grains have diameters in the range of 10 μm to 20 μm. Fig. 4 shows the microstructure of the induction-hardened specimen, B564, which contains only martensitic phase. The structure of this specimen is primarily lath, consistent with expectations for steel containing a few tenths of a percent carbon [8].

Fig. 5 shows the measured frequency spectrum for the martensitic specimen with an enlarged portion of a resonance. The results from Ritz calculation of the resonant frequencies are shown in the figure as vertical lines. The spectra of α-Fe and ferrite-pearlite specimens are not included here. Different dimensions of these specimens resulted in overall shifts in resonant frequencies, and the frequency ranges of the measured spectra correspondingly were shifted to include comparable numbers of modes for the Ritz analysis.

Fig. 6 shows the measured internal friction at each resonant frequency of the three specimens. The ferritic-pearlitic specimen

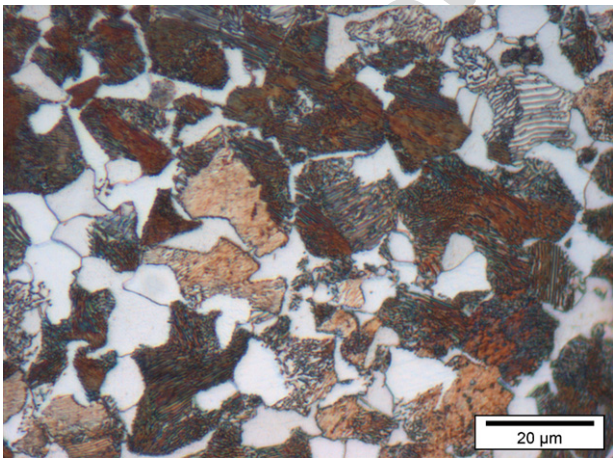

Fig. 3. Microstructure of specimen C322. White areas indicate grains of ferrite phase, and other grains contain pearlite. Grains are nearly equiaxed with an average diameter of about 10 μm.

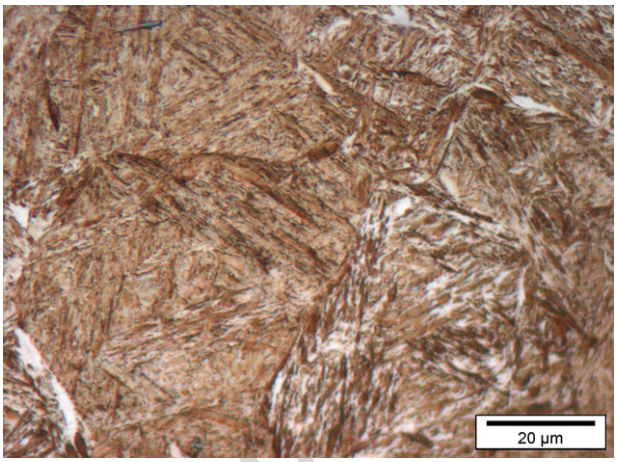

Fig. 4. Microstructure of specimen B564 showing predominantly lath martensite.

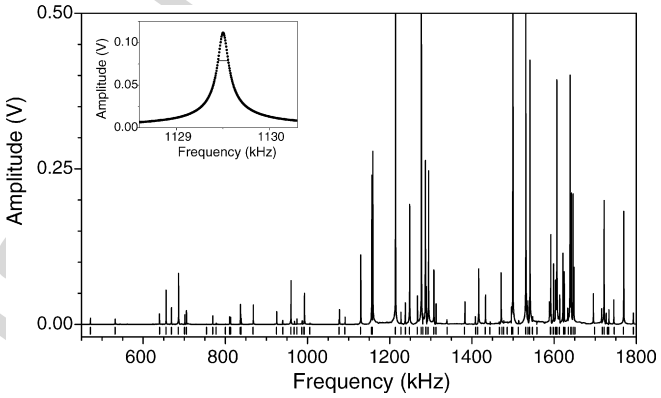

Fig. 5. Amplitude–frequency spectrum for martensite specimen. The bottom axis in the figure shows the calculated resonance frequencies as vertical bars. A magnified region shows a resonant peak and the width.

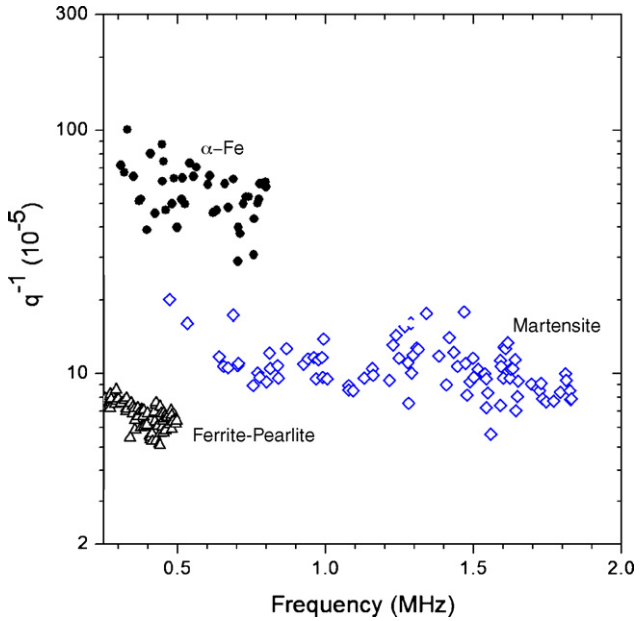

Fig. 6. Internal friction q_n^{-1} at each measured resonance in α-Fe, martensitic SAE 1050 steel, and ferritic-pearlitic SAE 1050 steel.

Table 1
Elastic constants and internal friction of induction hardened and unhardened plain carbon steel, SAE 1050

ij[a]	Martensite phase (Induction hardened)		Ferrite-pearlite phases (non-hardened)	
	C_{ij}	Q_{ij}^{-1} (10^{-5})	C_{ij}	Q_{ij}^{-1} (10^{-5})
11	268.1 ± 0.4	8.3 ± 1.3	273.4 ± 0.3	4.3 ± 1.3
22	268.4 ± 0.3	9.9 ± 1.1	273.2 ± 0.3	4.4 ± 1.0
33	267.2 ± 0.4	10 ± 1.2	274.3 ± 0.3	5.6 ± 1.2
44	79.06 ± 0.02	12 ± 0.6	82.15 ± 0.02	6.5 ± 0.5
55	78.72 ± 0.02	12 ± 0.7	82.05 ± 0.02	6.4 ± 0.5
66	78.85 ± 0.03	8.9 ± 0.8	81.14 ± 0.01	7.7 ± 0.5
12	111.2 ± 0.3	8.6 ± 2.6	110.5 ± 0.2	−1.6 ± 2.3
13	110.2 ± 0.3	8.3 ± 2.6	110.8 ± 0.3	−1.7 ± 2.9
23	111.0 ± 0.2	9.5 ± 2.3	110.9 ± 0.2	1.8 ± 2.6
C_l	268.1	9.7	273.9	4.4
G	78.74	11	81.65	7.4
B	163.1	9.2	165.0	2.4
E	203.5	10	210.3	6.7
ν	0.2921		0.2877	

All units are in GPa, except for dimensionless internal friction and Poisson ratio. Polycrystalline values were estimated by averaging the orthorhombic C_{ij}, using the Voigt–Reuss–Hill [5–7] method.
[a] $x_3 \equiv$ along the axis of the shaft.

Table 2
α-Fe and averaged polycrystal elastic constants at room temperature

	C_{ij}	$Q_{ij}^{-1}(10^{-5})$	a	b	c	d	e	f	g	Avg. [a–g]
C_{11}	231.5 ± 0.5	28.1 ± 10.5	232.2	231.4	226	230.0	228	233.1	230.4	230 ± 3
C_{12}	135.0 ± 0.5	11.0 ± 18.7	135.6	134.7	140	134.6	132	135.5	134.1	135 ± 2
C_{44}	116.0 ± 0.08	67.1 ± 2.4	117.0	116.4	116	116.6	117	117.8	115.9 ± 0.2	117 ± 0.7
B	167.2 ± 0.3	18.9 ± 15.6	167.8	166.9	169	166.4	164	168.0	166.2 ± 0.9	167 ± 2
C'	48.23 ± 0.7	51.9 ± 10.7	48.3	48.35	43	47.7	48	48.8	48.15 ± 0.9	48 ± 2
C_l	276.8	35.5	278.0	276.9	274	275.9	274	279.2	275.6	276 ± 2
G	82.19	61.0	82.68	82.45	78.7	82.11	82.5	83.35	82.09	82.0 ± 1.5
E	211.9	55.0	213.0	212.4	204	211.5	212	214.6	211.5	211 ± 3
ν	0.2888	0.2884	0.2880	0.298	0.2881	0.285	0.2872	0.2879	0.289 ± 0.004	

All units are in GPa, except for dimensionless internal friction and Poisson ratio. Polycrystalline values were estimated by averaging the cubic C_{ij}, using the method of Kröner [6,7].
[a] Ref. [9].
[b] Ref. [10].
[c] Ref. [11].
[d] Ref. [12].
[e] Ref. [13].
[f] Ref. [14].
[g] Ref. [15].

shows the greatest dependence on frequency, but this dependence is still weak. These results show that the approximation of frequency independence of the internal friction in Eq. (1) is reasonable. In addition to the internal friction of the specimens, Fig. 6 contains contributions to the damping arising from the mechanical contact of the transducers. However, these contributions are expected to be small, considering that much lower values of internal friction in other metallic specimens have been measured with the same experimental configurations.

Table 1 lists orthorhombic elastic stiffnesses for the martensitic and ferritic-pearlitic specimens. These specimens show elastic anisotropies of 0.4% in the longitudinal stiffnesses and 0.06% to 1.2% in the shear stiffnesses as a result of microstructural texture and/or anisotropic dislocation arrays. Table 1 also lists the components of the internal friction Q_{ij}^{-1} and calculated isotropic elastic moduli and Poisson ratios. The uncertainties listed in the tables are estimated only from the standard deviation of the inverse Ritz calculation. (They do not include, for example, systematic errors arising from the approximation of frequency independence of the Q_{ij}^{-1}.)

Table 2 lists the elastic stiffness and internal friction determined for α-iron and, for comparison, values of elastic stiffnesses reported by other authors [9–15].

5. Discussion

5.1. Elastic constants

There is significant variation in the values reported in the literature for the elastic moduli of plain carbon steels and binary iron-carbon alloys with carbon content close to that of the specimens in the present study. Tables 3 and 4 summarize a number

Table 3
Polycrystalline elastic-moduli of ferritic-pealitic steel at room temperature

	Present	a	b	c	d
C_l	273.9	276.4			
E	210.3		211	187.5	189.6
G	81.65	82.76		73.2	

Units are in GPa.
[a] Ref. [16], ultrasonic pulse-echo measurement, 0.45 wt.% C.
[b] Ref. [17], quasi-static tensile tests, SAE 1050 steel.
[c] Ref. [18], dynamic resonance method, 0.48 wt.% C.
[d] Ref. [19], quasi-static tensile tests, 0.45 wt.% C.

of published values determined for ferritic-pearlitic and martensitic steels, respectively, using various techniques. To enable a direct comparison of results in these tables, we converted the longitudinal and shear velocities published in [16,20,21] to corresponding elastic moduli, using the measured densities of our ferritic-pearlitic and martensitic specimens.

Values for C_{11}, C_{12}, and C_{44} of α-Fe reported in [9–15] (Table 2) vary by a few percent. Our values in Table 2 are consistent with the average of these previously published values and agree most closely with those of Rotter and Smith [10].

The values of E and G that we determined for α-Fe (Table 2) are higher than those of ferrite-pearlite by 0.75% and 0.65%, respectively. Several effects are expected to contribute to these differences. The solubility of carbon in α-Fe is less than 1 carbon atom per 1000 iron atoms, and SAE 1050 contains carbon well above this solubility limit: approximately 1 carbon atom per 43 iron atoms. As a result, in the unquenched material, a large fraction of carbon atoms diffuse to form the pearlitic phase, which contains cementite. The elastic moduli of cementite [23], contrary to some reports [24–27], are expected to be stiffer than those of α-Fe. Carbon atoms that remain in the interstitial sites in the iron lattice are expected to increase the interatomic spring constants, which contributes to an increase in elastic moduli. However, interstitial carbon also increases the volume of the lattice, and this contributes to a reduction in elastic moduli. The dominant contribution among these competing effects apparently is the increase in volume induced by interstitials. Interstitials in face-centered cubic steel also have been reported to decrease elastic moduli through a similar volume effect [28].

Table 4
Polycrystalline elastic moduli of martensitic steel and binary Fe(C) at room temperature

	Present	a	b	c	d
C_l	268.1	267.9	264.3		
E	203.5			203	193.8
G	78.74	78.65	78.25		77.25
B	163.1				132.0

Units are in GPa.
[a] Ref. [20], ultrasonic pulse-echo measurement, water-quenched SAE 1040.
[b] Ref. [21], ultrasonic pulse-echo measurement, oil-quenched SAE 1050.
[c] Ref. [22], quasi-static tensile tests, SAE 1050.
[d] Ref. [23], ultrasonic pulse-echo measurement, Fe(0.5 wt.% C).

G, E, and B in the martensitic specimens are found to be, respectively, 3.6%, 3.2%, and 1.2% lower than in ferrite-pearlite. The interstitial volume effect, mentioned above, is expected to contribute to a lowering of these moduli. In addition, the greater concentration of dislocations in martensite affects the elastic moduli, since ultrasonic stress induces a reversible bowing of dislocations between pinning points [29,30]. Such movement is not induced in the dilatational mode, and this is consistent with the difference in B being less than that of E and G.

Although the microstructure of the martensite has much different grain shapes than those of the ferrite-pearlite, the degrees of elastic anisotropy are similar. Zener's anisotropy, defined as $A = 2C_{44}/(C_{11} - C_{12})$, is 1.01 for both ferrite-pearlite and martensite steel and 2.4 for α-Fe. A value of 1.0 for A represents a perfect isotropic solid.

5.2. Internal friction

In the isotropic approximation, the components of the internal friction of α-Fe are several times greater than those of the martensitic steel and approximately an order of magnitude greater than those of the ferritic-pearlitic steel. A determination of the physical basis of these differences is outside the scope of this study, since it would require extensive measurements as a function of temperature, frequency, and magnetic field. However, it may be useful to present several comments about possible mechanisms.

The damping in iron and steel at ambient temperatures is generally recognized to be dominated by dislocation and magnetomechanical mechanisms [31], with the intrinsic phonon-phonon [32] and thermoelastic [33] contributions being many orders of magnitude smaller. The magnitude of the dislocation contribution is proportional to the density of dislocations. For a single pinning length and frequencies below the high megahertz range, this contribution also is proportional, in the string model [29,30], to the ultrasonic frequency and the fourth power of the distance between pinning points, which mainly arise from point defects. However, in real materials with distributions of pinning lengths, the damping is typically much more weakly dependent on frequency.

The strong theoretical dependence of dislocation damping on the concentration of point-defects is consistent with our observation of greater damping in α-Fe. However, this dependence does not explain the damping being greater in martensite than in ferrite-pearlite, since martensite contains a greater concentration of carbon interstitials that pin dislocations. This greater damping may be explained by very high dislocation densities in lath martensite. For example, Morito et al. [34] measured dislocation concentrations of (1.4 to 3.2) $\times 10^{11}/\text{cm}^2$ for lath martensite of steel with carbon concentrations in the range of (0.4 to 0.6) wt.%. Dislocation concentrations in ferrite-pearlite are dependent on thermomechanical processing but, typically, are several orders of magnitude lower than those of martensite.

At ambient temperatures, zero applied magnetic field, and frequencies in the range of hundreds of kilohertz, there are two mechanisms of magnetomechanical damping that are expected

to be significant in ferromagnetic materials: microeddy-current and hysteretic [31,35]. The relative magnitude of these contributions depends on the size of magnetic domains and the mobility of domain walls, which are affected by thermomechanical processing [36]. Q^{-1} from microeddy currents is approximately proportional to frequency. Our measurements of frequency dependence for the three specimens (Fig. 6) are not consistent with microeddy-currents being the dominant contribution over the measured ranges of frequency. The hysteretic contribution is expected to be approximately independent of frequency in the low kilohertz range and to begin dropping at frequencies on the order of a megahertz. Therefore, the weak dependence on frequency shown in Fig. 6 is consistent with hysteretic damping being a significant contribution.

Table 1 provides evidence for significant damping Q_B^{-1} of hydrostatic waves (corresponding to the bulk modulus B) in martensite, while the values of Q_B^{-1} for ferrite-pearlite (Table 1) and monocrystalline iron (Table 2) are comparable only to the uncertainty in the least-squares analysis. Within the classical picture of anelastic point defects, no damping of hydrostatic waves is possible, because the degeneracy of differently oriented defects is not perturbed by hydrostatic stress [37]. Dislocation movement and associated damping also are induced only by shear stresses. On the other hand, since hydrostatic stress induces changes in temperature, such stress does induce thermoelastic damping. Although this mechanism can be the dominant damping for acoustic waves in liquid metals [38], it is again a relatively insignificant contribution in iron and steel. Generally, materials can have finite Q_B^{-1} if hydrostatic stress perturbs the spacing of nondegenerate energy levels of defects or the basic material structure and, therefore, induces thermally activated repopulation of these levels. Such a mechanism has been demonstrated, for example, in polymers [39,40]. We suggest that a defect-related mechanism of this general type may be responsible for the apparently finite Q_B^{-1} in steels.

6. Conclusions

1. All elastic moduli of ferrite-pearlite SAE 1050 steel are found to be lower than those of polycrystalline iron. This is attributed primarily to the increase in lattice volume induced by interstitial carbon.
2. The martensitic transformation induced by the induction hardening results in a lowering of shear, Young, and bulk moduli, and a raising of the Poisson ratio. The greatest effect was on the shear modulus, which decreased by ~3.6%. Since martensite has a greater concentration of interstitial carbon, the interstitial-induced increase in lattice volume again contributes to the reduction in moduli. Much higher concentrations of dislocations in martensite also may cause a significant reduction in moduli through reversible dislocation bowing.
3. The components of the internal friction of polycrystalline α-Fe are several times greater than those of the martensitic steel and approximately an order of magnitude greater than those of the ferritic-pearlitic steel. These differences are attributed primarily to the degree of pinning of dislocations by point defects and the density of dislocations.

Acknowledgements

Chris McCowan (National Institute of Standards and Technology) prepared the specimens for polishing and etching, and obtained photographs of the microstructures. Dr. Albert Migliori (Los Alamos National Laboratory) oriented and prepared the α-Fe specimen. Discussions with Dr. Hassel Ledbetter (Los Alamos National Laboratory) were helpful in interpreting the results.

References

[1] W.L. Johnson, S.A. Kim, S.J. Norton, in: D.O. Thompson, D.E. Chimenti (Eds.), Review of Progress in Quantitative Nondestructive Evaluation, 24B, AIP, Melville, NY, 2005, p. 1285.
[2] P. Heyliger, H. Ledbetter, M. Austin, Dynamic Elastic Modulus Measurements in Materials, Am. Soc. Test. Mat., Philadelphia, ASTM, STP1045, 1990, pp. 100–109.
[3] H. Demarest, J. Acoust. Soc. Am. 49 (1969) 768.
[4] A. Migliori, J. Sarrao, Resonant Ultrasound Spectroscopy, John Wiley & Sons, Inc, New York, 1997, pp. 53–59.
[5] R. Hill, Proc. Phys. Soc. (London) A65 (1952) 349.
[6] E. Kröner, Zeitschrift für Physik 151 (1958) 504–518.
[7] H. Ledbetter, Handbook of Elastic Proerties of Solids, Liquids, and Gases, III, Academic Press, San Diego, 2001, p. 313.
[8] W.C. Leslie, The Physical Metallurgy of Steels, McGraw-Hill, New York, 1981, p. 217.
[9] D.J. Dever, J. Appl. Phys. 43 (1972) 3293.
[10] C.A. Rotter, C.S. Smith, J. Phys. Chem. Solids 27 (1966) 267.
[11] J. Leese, A.E. Lord, J. Appl. Phys. 39 (1968) 3986.
[12] M. Guinan, D. Beshers, J. Phys. Chem. Solids 29 (1968) 541.
[13] A.E. Lord, D.N. Beshers, J. Appl. Phys. 36 (1965) 1620.
[14] J.A. Rayne, B.S. Chandrasekhar, Phys. Rev. 122 (1961) 1714.
[15] J.J. Adams, D.S. Agosta, R.G. Leisure, H. Ledbetter, J. Appl. Phys. 100 (2006) 113530–113537.
[16] J. Krautkrämer, H. Krautkrämer, Ultrasonic Testing of Materials, second ed., Springer-Verlag, New York, 1977, p. 527.
[17] M.L. Roessle, A. Fatemi, Int. J. Fatigue 22 (2000) 495–511.
[18] E.H.F. Date, J. Iron Steel Inst. (1969) 988–991.
[19] Y. Duyi, W. Zhenlin, Mater. Sci. Eng. A297 (2001) 54–61.
[20] C.H. Gür, B.O. Tuncer, Insight – Non-destructive Testing Condit. Monit. 47 (2005) 421–424.
[21] C.H. Gür, Y. Keleş, Insight – Non-destructive Testing Condit. Monit. 48 (2003) 615–620.
[22] G.R. Speich, A.J. Schwoeble, W.C. Leslie, Metal. Trans. 3 (1972) 2031–2037.
[23] H. Ledbetter, S. Kim, Elastic constants of cementite (Fe_3C), Mater. Sci. Eng. A, to be submitted.
[24] A.O. Miodownik, Mater. Sci. Techol. 10 (1994) 190–192.
[25] B.M. Drapkin, B.V. Fokin, Fiz. Met. Metalloved. 49 (1980) 649–651.
[26] B.M. Drapkin, G.M. Kimstach, D.A. Urtaev, Phys. Met. Metallog. 88 (1999) 594–597.
[27] L.A. Glikman, A.M. Kartashov, Z.M. Rubashkina, A.F. Lobov, Strength Mater. 7 (1975) 523–524.
[28] H. Ledbetter, M. Austin, Mater. Sci. Eng. 70 (1985) 143–149.
[29] J.S. Koehler, in: W. Shockley, J.H. Holloman, R. Maurer, F. Seitz (Eds.), Imperfections in Nearly Perfect Crystals, Wiley, New York, 1952, p. 197.
[30] A. Granato, K. Lücke, J. Appl. Phys. 27 (1956) 583.
[31] B.F. Coronel, D.N. Beshers, J. Appl. Phys. 64 (1988) 2006–2015.
[32] W. Mason, Physical Acoustics, IIIB, Academic, New York, 1965, p. 254.

[33] R. Yadav, D. Singh, J. Phys. Soc. Jpn. 70 (2001) 1825.
[34] S. Morito, J. Nishikawa, T. Maki, Iron Steel Inst. Jpn. 43 (2003) 1475–1477.
[35] A.S. Nowick, B.S. Berry, Anelastic Relaxation in Crystalline Solids, Academic Press, 1972, pp. 524–544.
[36] W.J. Bratina, in: W.P. Mason (Ed.), Physical Acoustics, Principles and Methods, IIIA, Academic, New York, 1966, pp. 223–291.
[37] A.S. Nowick, W.R. Heller, Adv. Phys. 14 (1965) 101–166.
[38] G.B. Webber, R.W.B. Stephens, in: WarrenP. Mason (Ed.), Physical Acoustics, IV, Part B, Academic Press, New York, 1968, p. 53.
[39] Y. Wada, R. Ito, H. Ochiai, J. Phys. Soc. Jn. 17 (1962) 213–218.
[40] N. Saito, K. Okano, S. Iwayangi, T. Hideshima, Solid State Physics, 14, Academic, New York, 1963, p. 343.